

pubs.acs.org/crystal Article

Supercell Formation in Epitaxial Rare-Earth Ditelluride Thin Films

Adrian Llanos, Salva Salmani-Rezaie, Jinwoong Kim, Nicholas Kioussis, David A. Muller, and Joseph Falson*



Cite This: Cryst. Growth Des. 2024, 24, 115-121



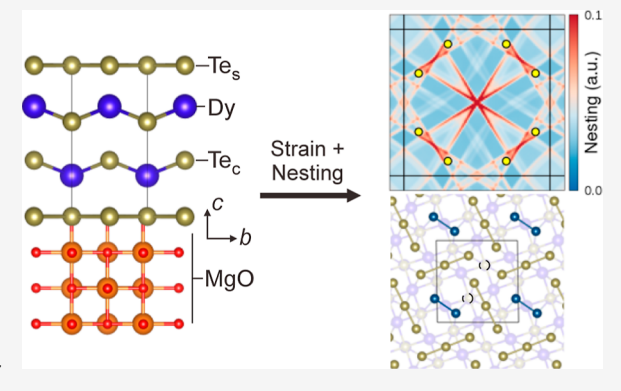
ACCESS I

Metrics & More

Article Recommendations

Supporting Information

ABSTRACT: Square-net tellurides host an array of electronic ground states and commonly exhibit charge-density-wave ordering. Here, we report the epitaxy of $\mathrm{DyTe}_{2-\delta}$ on atomically flat MgO (001) using molecular beam epitaxy. The films are single phase and highly oriented, as evidenced by transmission electron microscopy and X-ray diffraction measurements. Epitaxial strain is evident in films and is relieved as the thickness increases up to a value of approximately 20 quintuple layers. Diffraction features associated with a supercell in the films are resolved, which is coupled with Te-deficiency. First principles calculations attribute the formation of this defect lattice to nesting conditions in the Fermi surface, which produce a periodic occupancy of the conducting Te square-net and open a band gap at the chemical potential. This work establishes the groundwork for exploring the role of



strain in tuning the electronic and structural phases of epitaxial square-net tellurides and related compounds.

INTRODUCTION

Layered compounds sharing the square-net structural motif support a myriad of electronic phases including superconductivity,¹ topologically protected modes,² magnetism,^{3,4} and charge density waves (CDWs).⁵⁻⁷ Among this class of materials, rare-earth tellurides (LnTe_x, where Ln is a member of the lanthanide series and x = 2, 3 most commonly) have attracted attention due to the interplay between itinerant carriers and magnetism, superconductivity, and CDW-order. Sandwiched between corrugated quasi-ionic Ln-Te layers, the electronic structure of the covalently bonded two-dimensional square Te sheet can be conceptualized by a partially filled porbital manifold which obtains extra charge from an imbalance in valence states within the corrugated layer. 10,11 Modifying Ln acts to exert chemical pressure and influences the electronic properties of the material. For example, in the case of the rareearth tritellurides, chemical pressure acts to modify the CDW wavevector q, critical temperature, and the orthorhombicity of the crystal, ultimately revealing two orthogonal CDW with dissimilar ordering temperatures. 5,9

The related LnTe₂ display similar behaviors to the tritellurides but differ in key ways due to their electron filling of 7e-/Te in the square planar layers. ^{10,12} In contrast to the tritellurides, which form stoichiometric crystals, the ditellurides have a substantial width of formation and tend to form Tedeficient crystal structures with a range of stoichiometries and resulting superstructure modulations. ^{6,13-15} These modulations are often commensurate with the parent structure and have been shown in structurally refined crystal structure solutions ¹⁵⁻¹⁷ to result from an ordering of Te vacancies

within the Te sheet. However, incommensurate modulations have also been observed in LaTe $_{2-\delta}^{16}$ and CeTe $_{2-\delta}^{6}$. Electrical transport ranging from metallic to semiconducting ^{19,20} for similar nominal compositions and photoemission studies reporting both pseudogap ^{6,21} and fully gapped ²² Fermi surface structures further demonstrate the complexity of the ditelluride system. Superconductivity has also been reported in CeTe $_2$ at 0.2 GPa ²³ and in Sb-doped LaTe $_2$ at approximately 3 GPa. ²⁴ The subtle dependence on defect stoichiometry and applied pressure motivates an investigation into how their lattice and electronic structure evolve when crystals are synthesized in the thin-film form. Molecular beam epitaxy is a well-established method with which to fabricate ultrathin materials and probe the effects of substrate-induced strain. In this study, we use this technique to grow high-quality epitaxial rare-earth ditelluride thin films.

Here, we report the epitaxial growth of the rare-earth ditelluride $\mathrm{DyTe}_{2-\delta}$ on MgO (001) substrates. While little is known about $\mathrm{DyTe}_{2-\delta}$ in the bulk, the closely related structures of $\mathrm{LaTe}_{2-\delta}$ and $\mathrm{CeTe}_{2-\delta}^{-\delta}$ are reported to either have tetragonal or orthorhombic²⁵ symmetry belonging to the *P4/nmm* and *Pnma* space groups, respectively. We have found in all experiments that the ditelluride phase is stabilized

Received: June 23, 2023 Revised: November 16, 2023 Accepted: November 17, 2023 Published: December 13, 2023





preferentially over the tritelluride phase despite the synthesis being performed in Te-rich conditions. We attribute this to the weak van der Waals interactions between stacked Te-sheets on the surface of samples during layer-by-layer growth. While growth of the tritelluride phase has been reported in the ultrathin limit [<1 unit cell (u.c.)], this appears to not persist into multilayer films, even as thin as three quintuple layers (QLs).

Our results identify that epitaxial strain is evident in films and is dependent on the number of QL deposited, being progressively relieved as the films are made thicker. In the case of the P4/nmm structure adopted by DyTe2, a QL corresponds to a single unit cell. As will be discussed, because this unit cell is observed to distort such that the c-axis is doubled, we will henceforth describe the film thickness in numbers of QL to prevent ambiguity. The films are tetragonal within the detection limit of the X-ray diffraction apparatus. We additionally have resolved a commensurate superlattice in a subset of films with wave vectors $\mathbf{q}_1 = \frac{2}{5}\mathbf{a}^* + \frac{1}{5}\mathbf{b}^*$, $\mathbf{q}_2 = -\frac{1}{5}\mathbf{a}^* + \frac{2}{5}\mathbf{b}^*$, and $\mathbf{q}_3 = \frac{1}{2}\mathbf{c}^*$ where \mathbf{a}^* , \mathbf{b}^* , and \mathbf{c}^* are the reciprocal lattice vectors of the undistorted structure. In real space, this distortion can be thought of as $(\sqrt{5} \times \sqrt{5})$ $R26.6^{\circ} \times 2$ superlattice. In the case of ref 15, the distortion was associated with a reduction in symmetry of the compound from the P4/nmm to P4/n space group. The superlattice emerges due to a periodic Te-defect lattice, which also acts to open a gap in the electronic spectrum and induce semiconducting transport behavior. First principles calculations point toward nesting conditions of the Fermi surface at a qvector that corresponds to the $\sqrt{5} \times \sqrt{5}$ condition, suggesting that the formation of the defect lattice results from a similar driving force to the conventional picture of CDW formation where sections of the Fermi surface are gapped out by the formation of supercells with periodicity corresponding to the nesting condition.²⁷ The formation of off-stoichiometric crystals is, therefore, a thermodynamically favored process rather than an outcome of imperfect growth conditions. The calculations further reveal that a number of competing atomic arrangements may be present and dependent on the degree of strain in the crystal.

EXPERIMENTAL METHODS

Substrates are prepared by annealing in ultrahigh vacuum (base pressure $\approx\!10^{-10}$ Torr) using a home-built CO $_2$ laser heating apparatus, inspired by ref 28. We used MgO (001) (Crystec) substrates for growth without the back coating of an absorbing layer or additional cleaning steps. The combination of MgO (a = 0.421nm) and DyTe₂ (a = 0.429 nm) was selected due to the relatively good epitaxial relationship at approximately -1.9% mismatch, as shown in Figure 1a,b where we highlight the DyTe2 unit cell and its constituent atoms; sheet tellurium (Te_s), the corrugated layer tellurium (Te_c), and the rare-earth ion. Being hygroscopic, the MgO surface without annealing is of poor quality, but upon heating to 1140 °C we can generate step-terraced structures with an annealing time of 10 min²⁸ The substrate is then transferred to a dedicated telluride substrate holder in a glovebox and then reloaded into the vacuum cluster and transferred to the molecular beam epitaxy growth chamber. The reflected high energy electron diffraction (RHEED) signal from the surface remains qualitatively identical upon arrival into the growth chamber. Substrate heating in the growth chamber is provided by a conventional resistive SiC coil, and the temperature reported is read from a thermocouple between the substrate and the heating coil. Te was supplied using a thermal cracker cell with tank

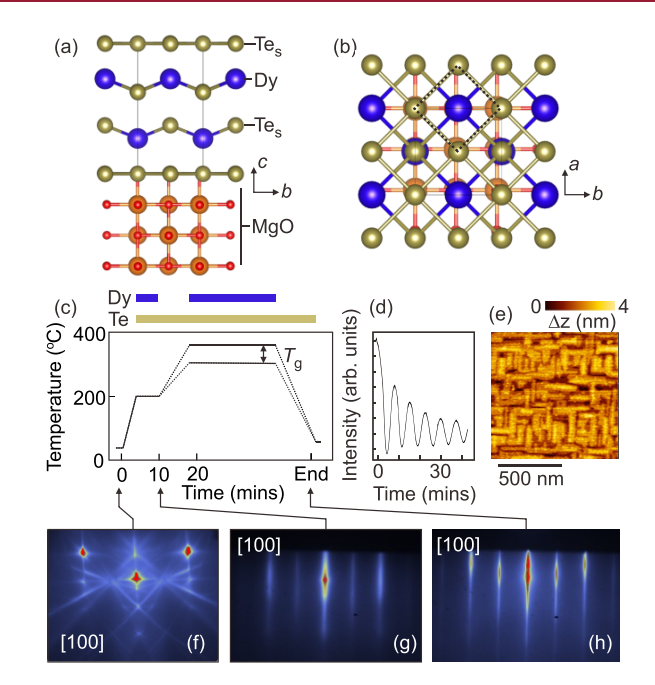


Figure 1. Crystal structure of DyTe₂ on MgO plotted along the (a) *a*-and (b) *c*-axis directions. (c) Schematic of the film growth recipe indicating substrate temperature as a function of time. Color bars at the top of the panel indicate when the Dy and Te effusion cells are open. (d) RHEED oscillations from the specular reflection of films as a function of growth time. (e) AFM image of a $T_{\rm g} = 330$ °C film of 20 QL RHEED of the (f) thermally prepared substrate, (g) after buffer layer deposition, and (h) at the conclusion of growth, all recorded along the [001] direction of the MgO substrate.

temperatures of approximately 450 °C and a cracking zone temperature of 1000 °C. Dysprosium was evaporated from a conventional effusion cell at a temperature of 1075 °C. We have found that both thermal cracking of Te and thermal preparation of substrates play a role in improving sample quality. Due to the air sensitivity of the films, we cap each film before extracting them from the vacuum chamber with either amorphous Ge or partially crystalline Te. This is performed in situ at $T\approx 90$ K using a liquid nitrogen cooling stage. X-ray diffraction data were obtained using a Rigaku Smartlab diffractometer using a 2-bounce Ge(220) monochromator. High-resolution diffraction employed copper K α 1 radiation. Grazing incidence diffraction of the (hk0) plane was accessed using an inplane diffraction arm with an incidence angle of $\omega\approx 0.35^\circ$. A 0.5° parallel slit collimator and 0.5° parallel slit analyzer were used to reduce in-plane beam divergence.

The cross-sectional scanning transmission electron microscopy (STEM) samples are prepared using a standard lift-out process on a Helios G4 UX DualBeam focused ion beam system. We utilize the Spectra 300 X-CFEG operating at 200 kV with a semiconvergence angle of 30 mrad and a high-angle annular dark-field (HAADF) detector with an angular range of 60-200 mrad to collect HAADF-STEM images. The HAADF-STEM images are acquired as a series of 25 images (250 ns per frame) and subsequently averaged to produce images with a high signal-to-noise ratio. STEM-energydispersive X-ray (EDX) spectroscopy data are acquired using a steradian Dual-X EDX detector, and the resulting spectrum is denoised through the application of the principal component analysis. We use an electron microscope pixel array detector to collect convergent beam electron diffraction (CBED) patterns at a convergence angle of 1.2 mrad and a dwell time of 1 ms. For the CBED simulation, we use the Py4DSTEM package based on the Bloch wave method.²⁹

Calculation Methods. The density functional theory calculations are performed using the Vienna *ab intio* simulation package^{30,31} with

the projector augmented wave method. The Dy-4f states are treated as core. All structures are optimized using the PBEsol exchange correlation functional, and the Bloch states are wannierized with the modified Becke-Johnson potential, which provides accurate band gaps, effective masses, and Frontierband ordering. The Fermi surfaces and nesting functions (Supporting Information) are obtained using the tetrahedron method with the Wannier Hamiltonian.

■ RESULTS AND DISCUSSION

The growth procedure is illustrated in Figure 1c. We begin with a low temperature ($T = 200 \, ^{\circ}\text{C}$) buffer layer on the annealed MgO surface. By observing intensity oscillations of the RHEED pattern, precise thickness control can be realized, allowing for the buffer layer growth to be stopped after a single QL. Attempts to grow films without a buffer layer resulted in poorly crystalline films, as observed by weak, diffuse features in RHEED. Growth of the remainder of the film takes place after annealing the buffer under Te flux to a final growth temperature. Growth rate is set by the flux of Dy atoms and was set at 1.2 Å/min for all growths under Te over pressure. The Te/Dy flux ratios were typically in the range of 10 to 20, corresponding to beam flux pressures of 7×10^{-9} mbar for Dy and 1.4×10^{-7} mbar for Te. We deposited films within a range of growth temperatures (T_g) , as shown in Figure 1c. For films deposited at low temperature ($T_g < 300$ °C), rough island growth appears, whereas those grown at elevated $(T_{\rm g} > 350~{\rm ^{\circ}C})$ overall suffer from poor crystallinity and rough surfaces, likely due to the low sticking coefficient of Te. RHEED oscillations during growth for moderate growth temperatures (T_g = 315 °C, Figure 1d) indicate that the film grows layer-by-layer with oscillations corresponding to the growth of a single unit cell. These oscillations were observed to decay after approximately 10 oscillations and were completely damped by the completion of a 20 QL thick film. To estimate the growth rate, we observed RHEED oscillations for the first several layers. The substrates are subsequently rotated at 5 RPM to enhance the sample uniformity. Figure 1e shows an atomic force microscopy image of the final surface of a 20 QL film, showing surface roughness on the order of 2-3 QL. RHEED images are shown of the pristine substrate (Figure 1f), after buffer layer (g) and postgrowth (h), the latter of which shows sharp, streaky patterns with prominent Kikuchi bands.

Transmission electron microscopy analysis is presented in Figure 2 and shows stacked layers of planar Te sheets and corrugated Dy-Te interlayers. The stacking sequence confirms the presence of the DyTe₂ phase and not DyTe₃. We attribute this to the low sticking coefficient of the Te-sheets, which evidently cannot be stacked in pairs (as is the case in the tritellurides), even with a Te/Dy flux ratio as high as 40. The film is phase pure with a sharp interface formed between the MgO and Te-square net sheet (Figure 2b). The squarenet tellurium sheet forms the first wet layer on the substrate. Rotated domains are evident in some areas of the film but are suppressed after a few monolayers of growth. The HAADF imaging (Figure 2a,b) and energy-dispersive X-ray spectroscopy elemental map (Figure 2c-e) show nominal (P4/nmm) DyTe₂ structure. The Dy/Te ratio with absorption and ionization cross-section corrections for the foil with a thickness of 30 nm is 0.497. This ratio, at its best, has a 10-20% error because of strong channeling.^{39,40} When the beam is along the zone axis, the intensity of the X-ray spectra is not a linear contribution of each element. The experimental CBED pattern (see the Supporting Information) matches the simulated CBED pattern of the (P4/nmm) space group when recorded along the [010] direction. The highresolution images also capture dissimilar intensities of Te sites along a line profile in the DyTe₂ [001] direction, as plotted in Figure 2f. The intensities of the Te columns at the Te sheet (Te_s) and the Te columns at the corrugated layer (Te_c) are different. We attribute this to the phase space for vibrations of the atoms in the square sheet versus those in the ionic Dy-Te layer; the higher thermal vibration in the Te sheets is an indication that the atoms are loosely bound. This observation is in agreement with our experience of being unable to

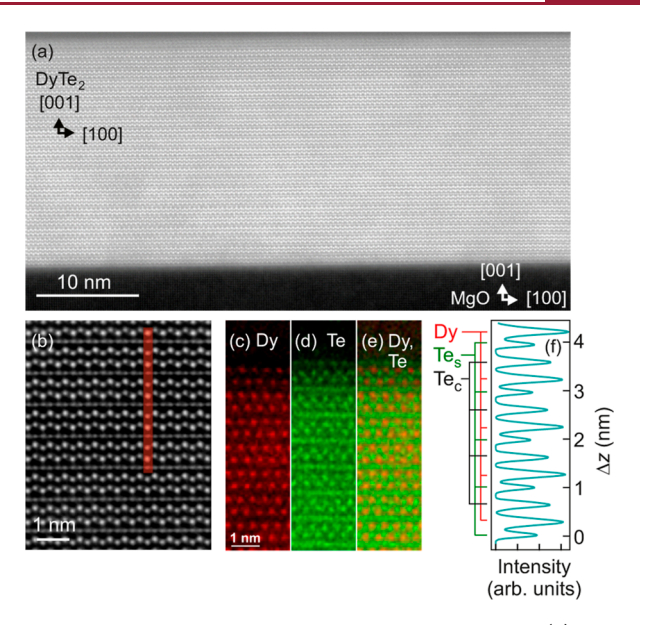


Figure 2. HAADF imaging of the film from a wide angle (a) and at the interface with MgO (b). (c, d) EDX mapping of the film showing occupancy of Dy and Te. (f) Intensity of atoms in a vertical line cut of the HAADF data indicated as the red bar in panel (b), showing the oscillatory intensity as a function of distance. The Dy, Te_s and Te_c sites are noted.

stabilize the tritelluride phase as a thin-film due to the poor sticking coefficient of Te atoms in the square net layer.

The structural properties of the grown films were further investigated using X-ray diffraction. Figure 3a shows a θ – 2θ scan, plotted in reciprocal lattice units (referenced to the P4/nmm DyTe₂ structure), showing highly c-axis oriented films with intense layer peaks accompanied by prominent Laue fringes indicating a high-quality film with a sharp interface with the underlying substrate. An ω rocking curve analysis of the DyTe₂ (003) peak produces a full-width at half-maximum (fwhm) of 0.03° , indicating low out-of-plane mosaicity. ϕ scan data (Figure S3) and reciprocal space mapping of the (hk0) plane (Figure 4a and Figure S4) taken in grazing incidence geometry after aligning to the [100] zone axis of the MgO substrate reveal the four-fold symmetry of the layer and further confirm the [100]_{DyTe₂}||[100]_{MgO} epitaxial relationship observed with RHEED. These data also reveal a weak diffraction spot from a domain oriented 30° relative to the [100] directions, indexed by a square in Figure 4a.

One goal of this work is to investigate the presence of epitaxial strain and its dependence on film thickness and growth parameters. To this end, we employ high-resolution reciprocal space mapping in the Q_x - Q_z plane for films with thicknesses between 3 and 35 QL. A characteristic data set for a 5 QL film is plotted in Figure 3c, showing the MgO (204) and DyTe_{2- δ} (208) diffraction spots. For the 3 QL cell film, the intensity in the $Q_x - Q_z$ plane was too weak to fit a peak. In this case, measurements of the $Q_x - Q_y$ RSM were performed about (hh0) for odd h layer diffraction peaks in grazing incidence geometry. These reflections were chosen to ensure that the MgO substrate would not contribute to the measurement. The c-axis lattice constants were determined from θ -2 θ measurements. In Figure 3d,e, we plot the evolution of the measured a and c lattice constants for films grown under a Te/Dy flux ratio of 20 and a growth temperature $T_{\rm g}$ = 310 °C. There is a continuous evolution of in-plane compressive strain from -1.1 to -0.5% relative to reported bulk values for DyTe_{1.8}. As will be described in the subsequent section, the presence of the observed superlattice implies that the stoichiometry is closest to DyTe_{1.8}, and the epitaxial strain estimates were referenced to these values. ¹⁵ The relaxed value of the in-plane lattice constant was found to be 4.26 Å. As expected for films showing in-plane compressive strain, the c-axis lattice constant was observed to evolve from +1.1% at the lowest thickness to +0.2% by 20 QL. Films grown at higher

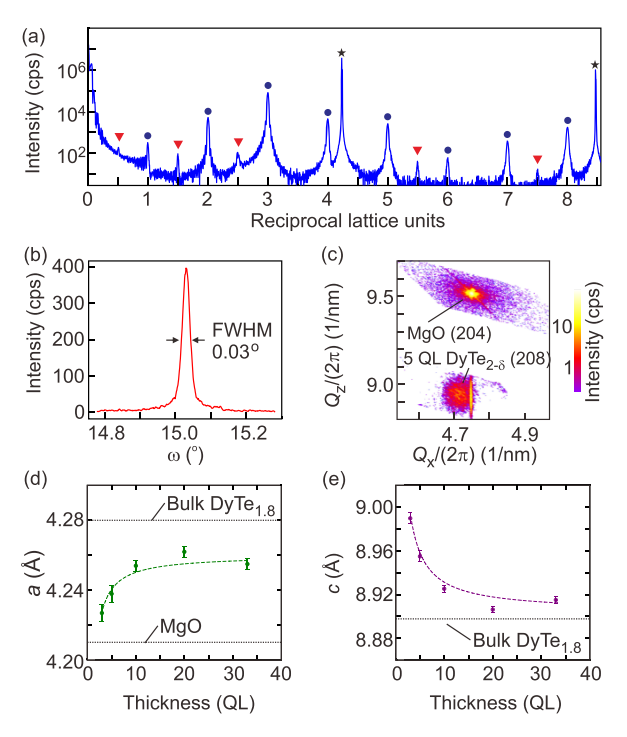


Figure 3. (a) Out-of-plane θ – 2θ X-ray diffraction of a 20 QL DyTe_{2- δ} film on MgO (001), plotted in reciprocal lattice units of DyTe_{2- δ}. Peaks corresponding to the substrate are indicated by a star, with fundamental peaks of the film labeled by a circle and superlattice peaks by a triangle. (b) Rocking curve analysis of the DyTe_{2- δ} (003) diffraction peak. (c) Out-of-plane asymmetric scan of the film with diffraction from the MgO (204) and DyTe_{2- δ} (208) planes plotted as a function of momentum transfer in the Q_x – Q_z plane. (d) In-plane a and (e) out-of-plane c lattice constants of films as a function of thickness compared with the values of ref 15. Dashed lines are intended as guides for the eye.

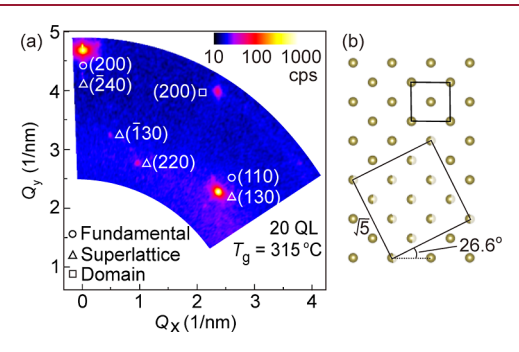


Figure 4. (a) In-plane (*hk*0) diffraction of a 20 QL film showing diffraction peaks identified as fundamental (circle) and superlattice (triangle). (b) Schematic of the Te square net layer showing the original square u.c. (upper square) and the distorted $\sqrt{5} \times \sqrt{5}$ R26.6° superlattice (lower rotated square) of partially occupied Tesites, indicated by half-transparent atoms.

temperatures ($T_{\rm g} > 330^{\circ}$) showed no evolution of strain with thickness.

It is known that in the case of La and Ce, the ditelluride structure is stable over a range of stoichiometries in the bulk, typically within the range of x = 1.8-2.0. The effects of such off-stoichiometries in the case of LaTe_{1.8} lead to a gap opening at the chemical potential. ^{16,17} The off-stoichiometries are known to produce a variety of structural modulations depending on Te deficiency. The most commonly observed modulation for the heavier rare earths (Gd, Tb, and Dy), ¹⁵ for a Te deficiency of 20%, was a $(\sqrt{5} \times \sqrt{5} \times 2)$ superlattice of the

LnTe $_2$ aristotype. The [100] axis of the ordered defect supercell is oriented parallel to the [210] direction of the higher symmetry parent structure. Such a defect modulation is reminiscent of that observed in the insulating phase of Fe-deficient FeSe 42 and in certain oxygen-deficient surface reconstructions of SrTiO $_3$.

Using grazing incidence X-ray diffraction, we are able to analyze the structural modulations present in $DyTe_{2-\delta}$ thin films, as shown in Figure 4a where we plot diffraction of a 20 QL film in the (hk0) plane. The enhanced intensity in grazing incidence geometry for thin films enables us to resolve the presence of the $\sqrt{5} \times \sqrt{5}$ modulation of the a-b plane, indexed by the diffraction spots identified by triangles in the figure, which are absent in the undistorted structure. In addition to these superlattice reflections, a reflection arising from rotation of the epilayer with respect to the substrate was also identified and is labeled in the figure with a square. A full phi scan of this (200) reflection is given in the Supporting Information along with TEM images of observed misoriented domains. Diffraction indices given by triangles are with respect to the full P4/n supercell [ICSD-130088 (ICSD release 2023.1)], whereas those identified by circles are referenced to the undistorted P4/nmm parent structure [ICSD-630332 (ICSD release 2023.1)]. 44 We refer to these as "superlattice" and "fundamental" reflections. The position of the (220) superlattice reflection relative to the (200) fundamental reflection indicates the presence of a rotated superlattice domain with modulation wavevector $\mathbf{q}_{1} = \frac{1}{5}\mathbf{a}^{*} + \frac{2}{5}\mathbf{b}^{*}, \ \mathbf{q}_{2} = \frac{2}{5}\mathbf{a}^{*} - \frac{1}{5}\mathbf{b}^{*}, \ \text{and} \ \mathbf{q}_{3} = \frac{1}{2}\mathbf{c}^{*}.$ Such a domain structure is expected due to the presence of mirror planes parallel to the a and b axes in the P4/nmm DyTe₂ parent structure. Domains form with [100] supercell axes aligning parallel to the [210] and $[2\overline{10}]$ directions of the parent structure, which, in the notation used in this paper, respectively, correspond to the $(\sqrt{5} \times \sqrt{5})$ R26.6° \times 2 and $(\sqrt{5} \times \sqrt{5})$ R63.4° \times 2 supercells. A similar arrangement of spots can be seen in the lower half of this quadrant of the (hk0) plane (Figure S4), consistent with the proposed domain structure. In the Supporting Information, we provide a table of indexed peaks and other relevant crystallographic information used in identifying the superlattice. θ - 2θ diffraction measurements revealed additional features at 0.5 reciprocal lattice units, which correspond to a doubling of the unit cell along the c-axis. Additionally in RHEED, we are able to resolve weak streaks associated with an in-plane modulation (see Figure S2). Taken all together, these diffraction features provide strong evidence for the $(\sqrt{5} \times \sqrt{5})$ R26.6° × 2 reconstruction being stabilized in the films. By comparing to the known modulations published for off-stoichiometric, bulk single-crystal DyTe $_{2-\delta^1}$ the presence of the defect lattice would imply an off-stoichiometry in the range of 10-20%, which is consistent with the EDX-obtained chemical ratios within the uncertainty of the measurement. All films with thicknesses greater than 10QL showed features consistent with the two-fold modulation of the c-axis. However, the comparably weaker diffracted intensity from films in the thin-limit combined with the intrinsically weak intensity from superlattice diffraction spots prevented the observation of the in-plane superlattice below 20 QL with our laboratory-based diffractometer.

To further understand the underlying origin of the experimentally observed supercell, we performed first principles calculations with and without Te deficiencies. Questions of interest include whether nesting within the Fermi surface promotes the formation of the supercell, the atomic arrangement within the supercell, and the resulting band structure of the extended compound. Figure 5 presents the main results of our calculations, and an extended set of data is available in the Supporting Information. The Fermi surface of the unmodulated pristine DyTe_{2- δ} structure at the chemical potential corresponding to δ = 0.2 Te deficiency is presented in Figure 5a, showing the Te_s pand the Dy d-derived bands in blue and orange, respectively. The planar shapes of the Te_s-derived Fermi surface confirm their 2D nature. The presence of bands at the Fermi energy would be expected to produce metallic transport in films. However, we observe semiconducting transport with an activation gap on the order of 300 meV in a film of 20 QL (see the Supporting Information). Owing to the air sensitivity of the material, a reliable and systematic study of

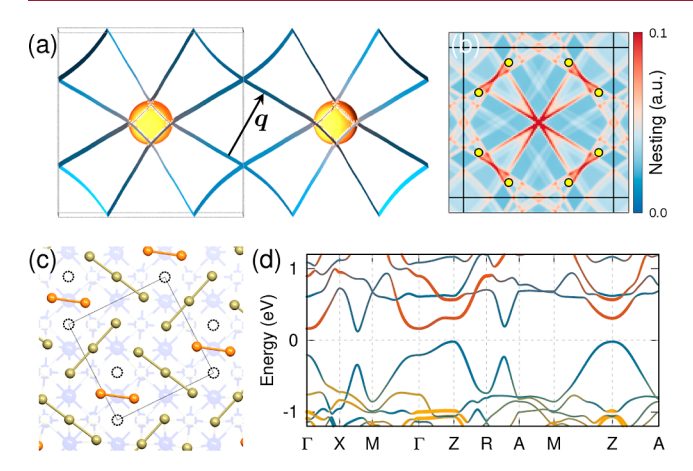


Figure 5. Density functional theory calculations of $\operatorname{DyTe}_{2-\delta}$: (a) Fermi surface of pristine DyTe_2 at a chemical potential corresponding to $\delta=0.2$ Te deficiency, where **q** is the nesting vector. (b) In-plane nesting function, $N_7(q_x,q_y)$ (see the Supporting Information), in the first Brillouin zone (solid lines), where the eight yellow dots denote the nesting vector **q**, corresponding to the $\sqrt{5} \times \sqrt{5}$ cell modulation. (c) Te bonding network for $\delta=0.2$ where the Te dimers are colored as orange. (d) Band structure along the symmetry directions of the $\sqrt{5} \times \sqrt{5}$ cell shown in (c) revealing the emergence of the band gap. The orbital characters of the Dy-d, Te_c-p, and Te_s-p-derived states in parts a and (d) are denoted by orange, yellow, and blue, respectively.

the activation gap with thickness as well as true measurements of the band gap could be obtained through in situ electrical and optical probes. While the gapping of the Fermi surface can be achieved through a number of means, in other square net compounds where CDW ground states have been identified, 5,25 a specific nesting vector q in momentum space may induce a maximal overlap of the 2D-like Fermi surfaces, which allows energy gain from the band gap opening near the Fermi level, though this picture has been debated.⁴⁸ However, the interpretation of CDW using the nesting mechanism can also be applied to defect formation. In sharp contrast to randomly distributed defects, the defect lattice induces cell modulation where the energy gain is derived from a gapping of the Fermi surface at a specific q-vector which gives maximal Fermi surface overlap. The calculated nesting function, $N(\mathbf{q})$ (see the Supporting Information), of the Fermi surface in Figure 5a is displayed in Figure 5b, where red colors indicate wavevectors with a strong nesting condition at the Fermi energy. The yellow dots correspond to the q-vector which would produce a $\sqrt{5} \times \sqrt{5}$ modulation, and they are seen to closely coincide with the nesting conditions of the Fermi surface. Therefore, we hypothesize that the $\sqrt{5} \times \sqrt{5}$ modulation is promoted in the structure to minimize energy. However, in contrast to the purely electronic CDW-order, it appears likely that the crystal preferentially forms a defect lattice. Removal of a Te from the square net sheet effectively contributes extra charge to the layer, in turn localized on the periodic defect site, as there are no states from the DyTe slab at the Fermi level. Interestingly, the nesting function at the Fermi level of the pristine structure (Figure S5d) exhibits its peaks at q-vectors shorter than that of $\sqrt{5} \times \sqrt{5}$ modulation. This implies that the formation of a defect lattice is a consequence of the mutual effects of the charge doping and the nesting function at the altered chemical potential. The question remains what the defect lattice looks like locally and how it influences the formation energy and the band structure. Consequently, we have carried out calculations of the $\sqrt{5}$ \times $\sqrt{5}$ supercell with Te_s mono- and divacancies corresponding to δ = 0.1 and 0.2. We find that the A–C divacancy configuration, consisting of Te_s dimers and trimers, as shown in Figure 5c, has the lowest formation energy among the five considered structures and is in agreement with previous X-ray diffraction measurements on SmTe_{1.8}. 46 This configuration is favored in the calculations when the a-axis lattice parameter is compressed, which is a trend that is resolved

in diffraction in Figure 3d and could explain why the relaxed lattice constants of grown film are smaller than their bulk counterparts. 15 The band structure of the A-C configuration along symmetry directions, as shown in Figure 5d, demonstrates the emergence of a band gap (indirect gap of 143 meV and direct gap of 326 meV), which is of the same order of magnitude as the activation gap measured in transport. We also find a band gap for the monovacancy and A-B divacancy configurations, while the A-D divacancy configuration with a higher formation energy is metallic (see the Supporting Information for the calculated band structures and the band gaps.) Therefore, we speculate that these vacancy configurations, especially A-C, are stabilized and are responsible for the semiconducting transport behavior. Additional structure modulation along the c-direction is also reproduced under the assumption of the dominant δ = 0.2 A–C configuration. The calculated total energies of the $\sqrt{5}$ \times $\sqrt{5}$ \times 2structure (Supporting Information Table S1) show that the A-C divacancy appears at a laterally displaced position (0.5 and 0.5), relative to the divacancy on the adjacent Te square net layer. This lateral displacement lowers the total energy by approximately 10 meV/Dy compared to the $\sqrt{5} \times \sqrt{5} \times 1$ structure, where the A-C dimers align as a column.

CONCLUSIONS

In summary, we have grown epitaxial DyTe $_{2-\delta}$ on atomically flat MgO surfaces, which induces compressive strain in the films. The in-plane lattice constant of the films increases as the thickness is increased, indicating a relieving of strain. The high structural quality of films enables detection of a $\sqrt{5} \times \sqrt{5} \times 2$ R26.6° superlattice in diffraction. While an electronically driven CDW does not appear to be relevant to understanding the properties of this system, first principles calculations point toward nesting in the Fermi surface as a possible mechanism for promoting the supercell modulation, which in turn produces a band gap and semiconducting transport. This work sets the stage for studying the role epitaxial strain has on the broader class of LnTe $_{2-\delta}$ and related square net compound, and ultimately their heterointerfaces.

ASSOCIATED CONTENT

Supporting Information

The Supporting Information is available free of charge at https://pubs.acs.org/doi/10.1021/acs.cgd.3c00755.

Off-axis RHEED image with saturated brightness showing weak additional streaks which we tentatively associated with the $\sqrt{5} \times \sqrt{5}$ modulation; RHEED images taken at the end of growths performed in the indicated temperature windows; ϕ scan around the (200) diffraction condition; STEM images of rotated domains; RSM of the lower half of the first quadrant of the (hk0) plane; temperature-dependent transport of a 20 QL film showing semiconducting transport; CBED pattern and simulated CBED pattern of the (P4/nmm) point group; electronic structure of pristine DyTe₂; calculated total energies for the $\sqrt{5} \times \sqrt{5} \times 2$ supercell structures with A-C divacancy configuration; calculated band structures along the high symmetry directions for the $\sqrt{5} \times \sqrt{5}$ supercell with several vacancy configurations; observed (hk0) reflections with comparison to bulk crystal report; and calculated total energies for the $\sqrt{5} \times \sqrt{5} \times 2$ supercell structures with A–C divacancy configuration (PDF)

AUTHOR INFORMATION

Corresponding Author

Joseph Falson — Department of Applied Physics and Materials Science and Institute for Quantum Information and Matter, California Institute of Technology, Pasadena, California 91125, United States; Ocid.org/0000-0003-3183-9864; Email: falson@caltech.edu

Authors

- Adrian Llanos Department of Applied Physics and Materials Science and Institute for Quantum Information and Matter, California Institute of Technology, Pasadena, California 91125, United States
- Salva Salmani-Rezaie School of Applied and Engineering Physics and Kavli Institute at Cornell for Nanoscale Science, Cornell University, Ithaca, New York 14853, United States
- Jinwoong Kim − Department of Physics and W. M. Keck Computational Materials Theory Center, California State University, Northridge, Northridge, California 91330, United States; © orcid.org/0000-0003-3616-865X
- Nicholas Kioussis Department of Physics and W. M. Keck Computational Materials Theory Center, California State University, Northridge, Northridge, California 91330, United States
- David A. Muller School of Applied and Engineering Physics and Kavli Institute at Cornell for Nanoscale Science, Cornell University, Ithaca, New York 14853, United States

Complete contact information is available at: https://pubs.acs.org/10.1021/acs.cgd.3c00755

Notes

The authors declare no competing financial interest.

ACKNOWLEDGMENTS

We thank Kaveh Pezeshki for help in the early stages of this project, Keisuke Saito for help with diffraction measurements, and appreciate discussions with Ian Fisher, Leslie Schoop, and Anshul Kogar. J.F. acknowledges funding provided by the Air Force Office of Scientific Research (grant number FA9550-22-1-0463), partial funding provided by the Gordon and Betty Moore Foundation's EPiQS Initiative (grant number GBMF10638), and the Institute for Quantum Information and Matter, an NSF Physics Frontiers Center (NSF grant PHY-1733907). We also acknowledge the Beckman Institute for their support of the X-Ray Crystallography Facility at Caltech. N.K. and J.F. acknowledge support from the NSF-PREP CSUN/Caltech-IQIM Partnership (grant number 2216774) and NSF-PREM (grant number DMR-1828019). This work made use of a Helios FIB supported by NSF (grant no. DMR-1539918) and the Cornell Center for Materials Research (CCMR) Shared Facilities, which are supported through the NSF MRSEC Program (grant no. DMR-1719875). The Thermo Fisher Spectra 300 X-CFEG was acquired with support from PARADIM (NSF MIP DMR-2039380) and Cornell University. S.S.R. acknowledges the support of the Kavli and PARADIM fellowship.

REFERENCES

(1) Zhang, W. H.; Sun, Y.; Zhang, J. S.; Li, F. S.; Guo, M. H.; Zhao, Y. F.; Zhang, H. M.; Peng, J. P.; Xing, Y.; Wang, H. C.; et al. Direct Observation of High-Temperature Superconductivity in One-Unit-Cell FeSe Films. *Chin. Phys. Lett.* **2014**, *31*, 017401.

- (2) Klemenz, S.; Lei, S.; Schoop, L. M. Topological Semimetals in Square-Net Materials. *Annu. Rev. Mater. Res.* **2019**, *49*, 185–206.
- (3) Sankar, R.; Muthuselvam, I. P.; Babu, K. R.; Murugan, G. S.; Rajagopal, K.; Kumar, R.; Wu, T.-C.; Wen, C.-Y.; Lee, W.-L.; Guo, G.-Y.; Chou, F.-C. Crystal Growth and Magnetic Properties of Topological Nodal-Line Semimetal GdSbTe with Antiferromagnetic Spin Ordering. *Inorg. Chem.* **2019**, *58*, 11730–11737.
- (4) Lei, S.; Teicher, S. M. L.; Topp, A.; Cai, K.; Lin, J.; Cheng, G.; Salters, T. H.; Rodolakis, F.; McChesney, J. L.; Lapidus, S.; et al. Band Engineering of Dirac Semimetals Using Charge Density Waves. *Adv. Mater.* **2021**, 33, 2101591.
- (5) Ru, N.; Condron, C. L.; Margulis, G. Y.; Shin, K. Y.; Laverock, J.; Dugdale, S. B.; Toney, M. F.; Fisher, I. R. Effect of chemical pressure on the charge density wave transition in rare-earth tritellurides RTe₃. Phys. Rev. B: Condens. Matter Mater. Phys. 2008, 77, 035114.
- (6) Shin, K. Y.; Brouet, V.; Ru, N.; Shen, Z. X.; Fisher, I. R. Electronic structure and charge-density wave formation in LaTe_{1.95} and CeTe_{2.00}. Phys. Rev. B: Condens. Matter Mater. Phys. **2005**, 72, 085132.
- (7) Lei, S.; Duppel, V.; Lippmann, J. M.; Nuss, J.; Lotsch, B. V.; Schoop, L. M. Charge Density Waves and Magnetism in Topological Semimetal Candidates $GdSb_xTe_{2-x-\delta}$. Adv. Quantum Technol. **2019**, 2, 1900045.
- (8) Lei, S.; Lin, J.; Jia, Y.; Gray, M.; Topp, A.; Farahi, G.; Klemenz, S.; Gao, T.; Rodolakis, F.; McChesney, J. L.; et al. High mobility in a van der Waals layered antiferromagnetic metal. *Sci. Adv.* **2020**, *6*, No. eaay6407.
- (9) Yumigeta, K.; Qin, Y.; Li, H.; Blei, M.; Attarde, Y.; Kopas, C.; Tongay, S. Advances in Rare-Earth Tritelluride Quantum Materials: Structure, Properties, and Synthesis. *Adv. Sci.* **2021**, *8*, 2004762.
- (10) Tremel, W.; Hoffmann, R. Square nets of main-group elements in solid-state materials. *J. Am. Chem. Soc.* **1987**, *109*, 124–140.
- (11) Hoffmann, R. Solids and Surfaces: A Chemist's View of Bonding in Extended Structures; VCH Publishers, 1988.
- (12) Kikuchi, A. Electronic Structure of Lanthan Ditellurides. J. Phys. Soc. Jpn. 1998, 67, 1308–1312.
- (13) Niihara, K.; Shishido, T.; Yajima, S. The Nonstoichiometry of Gadolinium Ditelluride. *Bull. Chem. Soc. Jpn.* **1972**, 45, 1239–1240.
- (14) Park, S.-M.; Park, S.-J.; Kim, S.-J. The Superstructure of Semiconducting SmTe_{2-x}. *J. Solid State Chem.* **1998**, *140*, 300–306.
- (15) Poddig, H.; Donath, T.; Gebauer, P.; Finzel, K.; Kohout, M.; Wu, Y.; Schmidt, P.; Doert, T. Rare Earth Metal Polytellurides RETe_{1.8} (RE = Gd, Tb, Dy), Directed Synthesis, Crystal and Electronic Structures, and Bonding Features. *Z. Anorg. Allg. Chem.* **2018**, *644*, 1886–1896.
- (16) Poddig, H.; Finzel, K.; Doert, T. LaTe_{1.82(1)}: modulated crystal structure and chemical bonding of a chalcogen-deficient rare earth metal polytelluride. *Acta Crystallogr., Sect. C: Struct. Chem.* **2020**, *76*, 530–540.
- (17) Poddig, H.; Gebauer, P.; Finzel, K.; Stowe, K.; Doert, T. Structural Variations and Bonding Analysis of the Rare-Earth Metal Tellurides RETe_{1.875± δ} (RE = Ce, Pr, Sm, Gd; 0.004 $\leq \delta \leq$ 0.025). *Inorg. Chem.* **2021**, *60*, 11231–11241.
- (18) Stöwe, K. Crystal Structure and Electronic Band Structure of LaTe₂. J. Solid State Chem. **2000**, 149, 155–166.
- (19) Jung, M.; Kwon, Y.; Suzuki, T. Transport properties of CeTe₂. *Phys. B* **1997**, 240, 83–87.
- (20) Kwon, Y.; Min, B. Anisotropic transport properties in RTe_2 (R: La, Ce, Pr, Sm and Gd). *Phys. B* **2000**, 281-282, 120-121.
- (21) Chung, J.; Park, J.; Park, J. G.; Choi, B.-H.; Oh, S. J.; Cho, E. J.; Kim, H. D.; Kwon, Y. S. Photoemission Study of Rare-Earth Ditelluride Compounds (ReTe₂: Re = La, Pr, Sm, and Gd). *J. Korean Phys. Soc.* **2001**, *6*, 744.
- (22) Garcia, D. R.; Gweon, G.-H.; Zhou, S. Y.; Graf, J.; Jozwiak, C. M.; Jung, M. H.; Kwon, Y. S.; Lanzara, A. Revealing Charge Density Wave Formation in the LaTe₂ System by Angle Resolved Photoemission Spectroscopy. *Phys. Rev. Lett.* **2007**, *98*, 166403.
- (23) Jung, M. H.; Alsmadi, A.; Kim, H. C.; Bang, Y.; Ahn, K. H.; Umeo, K.; Lacerda, A. H.; Nakotte, H.; Ri, H. C.; Takabatake, T.

Superconductivity in magnetically ordered CeTe_{1.82}. Phys. Rev. B: Condens. Matter Mater. Phys. 2003, 67, 212504.

- (24) Chen, X.; Sun, P.-h.; Xie, Z.; Meng, F.; Pei, C.; Qi, Y.; Ying, T.; Liu, K.; Guo, J.-g.; Chen, X. Pressure-induced superconductivity in charge-density-wave compound $\text{LaTe}_{2-x}\text{Sb}_x$ (x=0 and 0.4). arXiv (Condensed Matter.Superconductivity), September 16, 2022, 2209.07188, ver. 2. https://arxiv.org/abs/2209.07188.
- (25) DiMasi, E.; Foran, B.; Aronson, M. C.; Lee, S. Stability of charge-density waves under continuous variation of band filling in LaTe_{2-x}Sb_x (0 \leq x \leq 1). *Phys. Rev. B: Condens. Matter Mater. Phys.* **1996**, 54, 13587–13596.
- (26) Xu, Z.; Ji, S.-H.; Tang, L.; Wu, J.; Li, N.; Cai, X.; Chen, X. Molecular Beam Epitaxy Growth and Electronic Structures of Monolayer GdTe₃. *Chin. Phys. Lett.* **2021**, *38*, 077102.
- (27) Lee, S.; Foran, B. J. Defective Lattice Charge Density Waves in La₁₀Se₁₉, Cs₃Te₂₂, RbDy₃Se₈, and Dy_{65.33}Se₁₂₀. *J. Am. Chem. Soc.* **1996**, 118, 9139–9147.
- (28) Braun, W.; Jäger, M.; Laskin, G.; Ngabonziza, P.; Voesch, W.; Wittlich, P.; Mannhart, J. In situ thermal preparation of oxide surfaces. *APL Mater.* **2020**, *8*, 071112.
- (29) Savitzky, B. H.; Zeltmann, S. E.; Hughes, L. A.; Brown, H. G.; Zhao, S.; Pelz, P. M.; Pekin, T. C.; Barnard, E. S.; Donohue, J.; Rangel DaCosta, L.; et al. py4DSTEM: A Software Package for Four-Dimensional Scanning Transmission Electron Microscopy Data Analysis. *Microsc. Microanal.* **2021**, *27*, 712–743.
- (30) Kresse, G.; Furthmüller, J. Efficient iterative schemes for ab initio total-energy calculations using a plane-wave basis set. *Phys. Rev. B: Condens. Matter Mater. Phys.* **1996**, *54*, 11169–11186.
- (31) Kresse, G.; Furthmüller, J. Efficiency of ab-initio total energy calculations for metals and semiconductors using a plane-wave basis set. *Comput. Mater. Sci.* **1996**, *6*, 15–50.
- (32) Blöchl, P. E. Projector augmented-wave method. Phys. Rev. B: Condens. Matter Mater. Phys. 1994, 50, 17953–17979.
- (33) Kresse, G.; Joubert, D. From ultrasoft pseudopotentials to the projector augmented-wave method. *Phys. Rev. B: Condens. Matter Mater. Phys.* 1999, 59, 1758–1775.
- (34) Perdew, J. P.; Ruzsinszky, A.; Csonka, G. I.; Vydrov, O. A.; Scuseria, G. E.; Constantin, L. A.; Zhou, X.; Burke, K. Restoring the Density-Gradient Expansion for Exchange in Solids and Surfaces. *Phys. Rev. Lett.* **2008**, *100*, 136406.
- (35) Mostofi, A. A.; Yates, J. R.; Pizzi, G.; Lee, Y.-S.; Souza, I.; Vanderbilt, D.; Marzari, N. An updated version of wannier90: A tool for obtaining maximally-localised Wannier functions. *Comput. Phys. Commun.* **2014**, *185*, 2309–2310.
- (36) Marzari, N.; Mostofi, A. A.; Yates, J. R.; Souza, I.; Vanderbilt, D. Maximally localized Wannier functions: Theory and applications. *Rev. Mod. Phys.* **2012**, *84*, 1419–1475.
- (37) Becke, A. D.; Johnson, E. R. A simple effective potential for exchange. *J. Chem. Phys.* **2006**, *124*, 221101.
- (38) Tran, F.; Blaha, P. Accurate Band Gaps of Semiconductors and Insulators with a Semilocal Exchange-Correlation Potential. *Phys. Rev. Lett.* **2009**, *102*, 226401.
- (39) Lugg, N. R.; Kothleitner, G.; Shibata, N.; Ikuhara, Y. On the quantitativeness of EDS STEM. *Ultramicroscopy* **2015**, *151*, 150–159.
- (40) MacArthur, K. E.; Brown, H. G.; Findlay, S. D.; Allen, L. J. Probing the effect of electron channelling on atomic resolution energy dispersive X-ray quantification. *Ultramicroscopy* **2017**, *182*, 264–275.
- (41) Pietsch, U.; Holý, V.; Baumbach, T. High-Resolution X-ray Scattering: From Thin Films to Lateral Nanostructures, 2nd ed.; Advanced Texts in Physics; Springer: New York, 2004.
- (42) Liu, C.; Zou, K. Tuning stoichiometry and its impact on superconductivity of monolayer and multilayer FeSe on SrTiO₃. *Phys. Rev. B* **2020**, *101*, 140502.
- (43) Newell, D. T.; Harrison, A.; Silly, F.; Castell, M. R. SrTiO₃ (001)- $(\sqrt{5}\times\sqrt{5})$ -R26.6° reconstruction: A surface resulting from phase separation in a reducing environment. *Phys. Rev.* **2007**, *75*, 205429.

- (44) Pardo, M.; Flahaut, J.; Domange, L. Chimie Minerale-Les Tellurures des Elements des Terres Rares de Formule Generale MTe2. C. R. Hebd. Seances Acad. Sci. 1963, 256, 953.
- (45) Johannes, M. D.; Mazin, I. I. Fermi surface nesting and the origin of charge density waves in metals. *Phys. Rev. B: Condens. Matter Mater. Phys.* **2008**, *77*, 165135.
- (46) Ijjaali, I.; Ibers, J. A. Two new binary lanthanide polytellurides: Syntheses and crystal structures of CeTe_{1.90} and SmTe_{1.80}. *J. Solid State Chem.* **2006**, *179*, 3456–3460.